Chemical Science

ROYAL SOCIETY OF CHEMISTRY

EDGE ARTICLE

View Article Online
View Journal

Cite this: DOI: 10.1039/d5sc09544a

All publication charges for this article have been paid for by the Royal Society of Chemistry

Tailoring electrolyte activity for a highly stable LiOH redox process in lithium–oxygen batteries

Jiacheng Yang, Jiasen Guo, Zihong Wang, Bing-Qing Xiong, Jun Ma, Dazhuang Wang and Xiaodi Ren *

Lithium–oxygen (Li–O_2) batteries offer ultrahigh theoretical energy density, but suffer from limited cycle life and high overpotentials, particularly in LiOH-based systems. While LiOH chemistry provides superior environmental tolerance compared to Li_2O_2 systems, the inherent four-electron redox process creates substantial charging overpotentials that compromise performance. Here, we tailor electrolyte activity to enable an efficient LiOH redox process by integrating 1-phenylpyrrolidine (PPD) as a redox mediator within an ionic liquid electrolyte. PPD possesses an optimal oxidation potential and stable p–π conjugation, enabling homogeneous chemical decomposition of LiOH and overcoming electrode–electrolyte contact limitations. The ionic liquid 1-propyl-3-methylimidazolium bis(trifluoromethanesulfonyl)imide (C_3C_1im TFSI) is engineered to regulate water reactivity and maintain hydrogen-bond networks, thereby promoting selective LiOH formation over Li_2O_2 during discharge, while providing high oxidative stability to suppress mediator degradation—an issue prevalent in ether-based electrolytes. This electrolyte–mediator synergy shifts the charging mechanism from sluggish interfacial charge transfer to a fast, solution-mediated chemical route, delivering 180 stable cycles with markedly reduced overpotentials and ~10× longer cycle life. This work offers molecular-level design principles for tailoring electrolyte activity to achieve high-efficiency and durable Li–O_2 batteries based on LiOH chemistry.

Received 5th December 2025
Accepted 26th February 2026

DOI: 10.1039/d5sc09544a

rsc.li/chemical-science

Introduction

The increasing demand for high-energy-density storage systems has driven intensive research toward advanced battery technologies that can surpass the practical limitations of conventional lithium–ion batteries (250–300 Wh kg^{-1}).[1–3] Among the most promising candidates, lithium–oxygen (Li–O_2) batteries offer an exceptional theoretical gravimetric energy density of ~3500 Wh kg^{-1}, approaching that of hydrocarbon fuels and representing a transformative advancement for applications ranging from electric vehicles to grid-scale energy storage.[4,5] However, the realization of this potential requires addressing fundamental challenges related to reaction kinetics, cycling stability, and electrolyte compatibility that have hindered practical implementation.[6,7] Traditional Li–O_2 battery research has predominantly focused on Li_2O_2-based cathode chemistry, where oxygen reduction produces lithium peroxide as the primary discharge product.[8,9] While this approach has yielded significant insights, Li_2O_2-based systems face inherent limitations including poor electrical conductivity (10^{-9} mS cm^{-1}), sluggish decomposition kinetics, and aggressive reactivity toward organic electrolytes that generates parasitic products and compromises cycle life.[10,11] These challenges have motivated the exploration of alternative discharge chemistries, particularly LiOH-based systems that demonstrate superior environmental stability, enhanced CO_2 tolerance, and effective mitigation of superoxide-related side reactions through water addition.[1,12,13] The four-electron conversion pathway ($O_2 + 2H_2O + 4Li^+ + 4e^- \rightarrow 4LiOH$, $E^0 = 3.32$ V) offers thermodynamic advantages over Li_2O_2 formation while enabling operation in humid environments more representative of practical applications.[14–16] Despite these advantages, LiOH-based Li–O_2 batteries face challenges arising from the poor ionic and electronic conductivity of LiOH (1.99×10^{-5} mS cm^{-1} and 7.13×10^{-9} mS cm^{-1}, respectively).[17] The insulating nature of LiOH deposits creates substantial charge transfer barriers during oxygen evolution, resulting in high charging overpotentials and limiting energy efficiency.[18,19] Conventional mitigation strategies employing various catalysts have demonstrated modest improvements in charging kinetics.[9,20–23] However, these approaches remain constrained by fundamental limitations, including catalyst dissolution, poisoning effects, and their inability to transform the inherently electrochemical nature of LiOH oxidation, which requires direct four-electron transfer at the electrode interface.[24–26]

Hefei National Research Center for Physical Sciences at the Microscale CAS Key Laboratory of Materials for Energy Conversion, Department of Materials Science and Engineering, University of Science and Technology of China, Hefei, 230026, China. E-mail: xdren@ustc.edu.cn

Redox mediator strategies offer a paradigmatic shift by enabling chemical decomposition of discharge products through homogeneous solution-phase reactions, effectively decoupling product oxidation from electrode contact limitations.[27–30] In this mechanism, redox mediators undergo electrochemical oxidation at the electrode surface, then diffuse into the electrolyte to chemically react with LiOH deposits, regenerating the mediator while producing O_2.[29] While several mediators have proven effective for Li_2O_2 systems, the application of such a strategy to LiOH-based chemistry remains largely unexplored, particularly regarding the critical issue of mediator-electrolyte compatibility at the elevated potentials required for LiOH oxidation (>3.32 V). This study addresses this gap by introducing 1-phenylpyrrolidine (PPD) as a novel redox mediator specifically designed for LiOH systems, featuring a well-matched oxidation potential (3.55 V) and stable p–π conjugated structure. Recognizing that traditional ether solvents demonstrate susceptibility to superoxide attacks and insufficient oxidative stability for high-potential mediator operation, we employ ionic liquid electrolytes with high stability with superoxide and wide electrochemical windows to ensure mediator-solvent compatibility. It is worth noting that the interactions between the ionic liquid and LiTFSI could preserve the hydrogen-bonding network and the reactivity of water, thereby promoting selective LiOH formation over Li_2O_2 during discharge and providing enhanced oxidation stability to avoid electrolyte degradation. Through systematic experimental validation and theoretical analysis, we demonstrate that the synergistic combination of redox mediator molecular design and solvent engineering enables significantly enhanced cycling stability (180 cycles) with reduced charging overpotentials, establishing design principles for redox mediator implementation in next-generation LiOH-based Li–O_2 batteries.

Results and discussion

The core principle underlying redox mediator functionality involves the oxidation of the mediator near the electrode surface during charging, followed by the diffusion of the oxidized species through the electrolyte to chemically react with discharge products.[7,31] This mechanism enables the decomposition of LiOH deposits that are physically separated from the electrode surface, thereby addressing the fundamental contact limitations that plague traditional catalytic approaches. However, the successful implementation of this strategy requires careful consideration of the redox potential matching between the mediator and target discharge product, and critically, the compatibility between the oxidized mediator species and the electrolyte solvent system.[29,32]

Our molecular design strategy centers on PPD as the redox mediator specifically tailored for LiOH-based systems. The selection of PPD is predicated on its redox potential, which appropriately exceeds the theoretical formation voltage of LiOH (3.32 V) and maintains an optimal energy efficiency margin. The molecular architecture of PPD features a p–π conjugation system between the nitrogen atom and benzene ring, which ensures structural stability during oxidation processes and facilitates reversible electron transfer. This conjugated structure enables PPD to maintain its molecular integrity upon oxidation to PPD^+, as shown in Fig. 1a, thereby supporting sustained redox mediator functionality throughout extended cycling. The PPD^+ generated through oxidation readily engages in a redox reaction with OH^- within the system, oxidizing OH^- while being reduced back to PPD, thus completing a reversible redox cycle that is crucial for maintaining the overall electrochemical performance and stability of the system. The critical importance of solvent compatibility emerges from the recognition that oxidized redox mediator species must remain chemically stable within the electrolyte environment to prevent parasitic reactions that compromise cycling performance. Traditional ether-based solvents, while exhibiting favorable ionic conductivity and oxygen diffusion properties, are likely to suffer from insufficient oxidation stability when exposed to highly oxidizing species such as PPD^+.[33] This incompatibility leads to irreversible electrolyte degradation and progressive loss of redox mediator functionality. To address this fundamental limitation, we employ ionic liquids as alternative electrolyte solvents, leveraging their characteristically wide electrochemical windows and superior oxidative stability to maintain compatibility with oxidized redox mediator species.[34,35] Among various ionic liquid candidates, 1-propyl-3-methylimidazolium ($C_3C_1im^+$) was selected as the ionic liquid cation due to its good ionic conductivity,[35] established excellent electrochemical stability (>5 V stability window) and favorable oxygen electrochemistry.[36,37] Density functional theory (DFT) calculations were performed to examine the oxidation and reduction stability of C_3C_1im TFSI in comparison to the traditional ether solvent tetraethylene glycol dimethyl ether (TEGDME) (Fig. 1b and Table S1). PPD has a higher highest occupied molecular orbital (HOMO) energy (−5.15 eV) than other electrolyte components, favoring direct electron transfer during the charging process. Conversely, TEGDME exhibits a higher HOMO than PPD^+ (−7.04 eV *vs.* −7.33 eV). This unfavorable energy alignment creates a thermodynamic driving force of approximately 0.29 eV for TEGDME oxidation by PPD^+, leading to irreversible consumption of both the redox mediator and solvent, consistent with the previous reports.[33] In contrast, C_3C_1im TFSI possesses lower HOMOs than PPD^+, indicating their ability to remain stable in the oxidative environment of PPD^+. Linear scanning voltammetry (LSV) revealed that C_3C_1im TFSI maintains exceptional electrochemical stability up to approximately 5.0 V *versus* Li/Li^+, significantly higher than that of TEGDME (which is stable up to ∼4.5 V), providing an adequate stability margin for redox mediator operation at elevated potentials (Fig. 1c). This wide electrochemical window results from the robust bis(trifluoromethanesulfonyl)imide anion and the electron-deficient imidazolium cation, both of which resist oxidative decomposition through their electron-withdrawing substituents and aromatic stabilization.[37,38]

As the proton source of the discharge product LiOH, H_2O was introduced into the electrolyte. To avoid the interference from the side reactions between lithium metal and water that can lead to parasitic hydrogen evolution and electrolyte decomposition, $LiFePO_4$ electrodes were employed as the counter

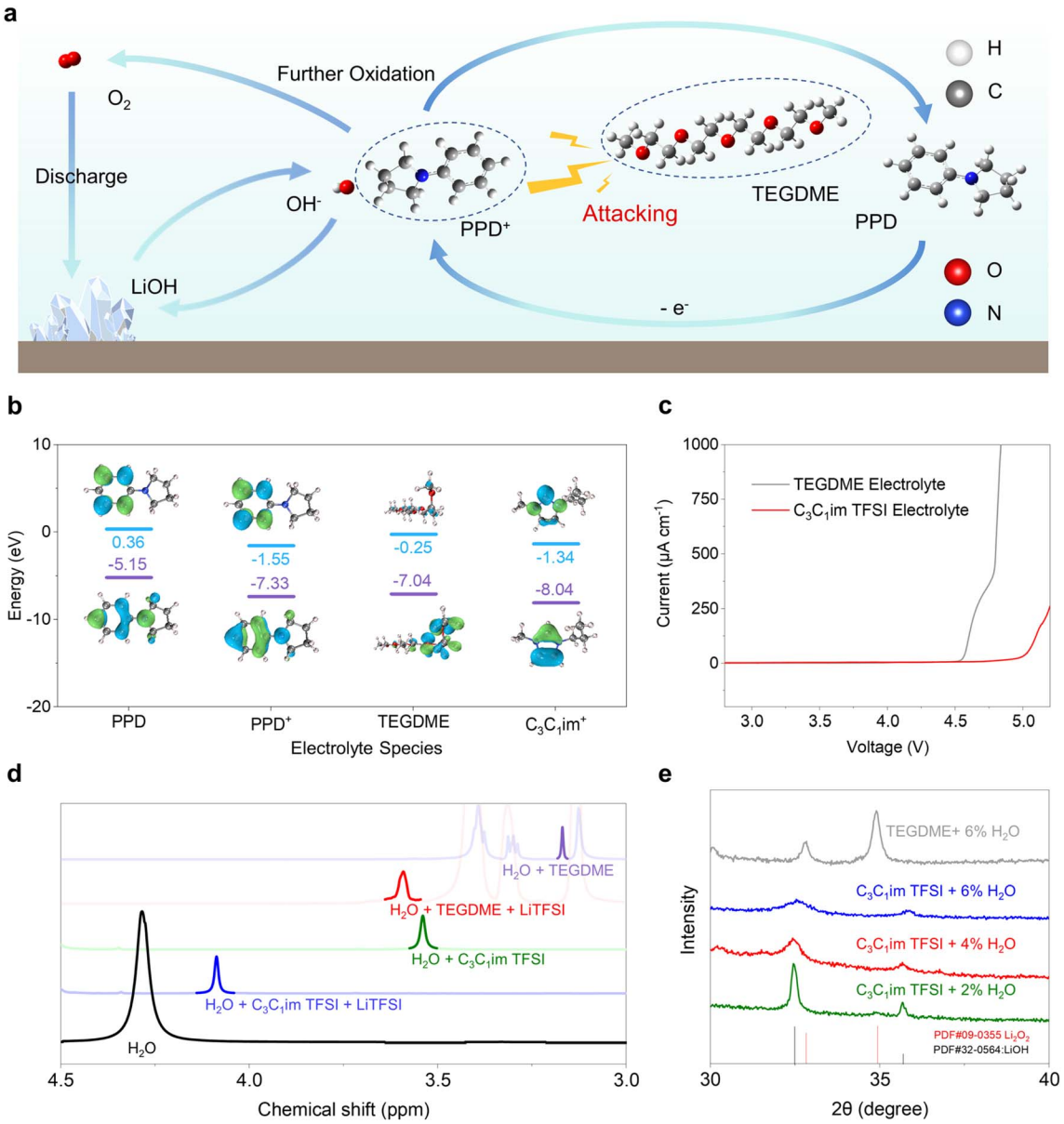

Fig. 1 (a) The schematic diagram of the mechanism of PPD and potential degradation of TEGDME. (b) The LUMO and HOMO values of various molecules in the electrolyte. (c) LSV curves of different electrolytes with 0.5 M LiTFSI on SP-PVDF electrodes. (d) ^{1}H NMR spectra of H_2O in different solvents. (e) XRD patterns of discharged cathodes with 0.5 M LiTFSI and different H_2O content in C_3C_1im TFSI-based and TEGDME-based electrolytes.

electrode. This substitution enables systematic investigation of cathode chemistry without complications from anode-water interactions while maintaining electrochemical relevance. The $LiFePO_4$ system demonstrated stable discharge and charge plateaus at approximately 3.45 V *versus* Li/Li^+ (Fig. S1). ^{1}H-NMR was employed to elucidate the interactions between H_2O and C_3C_1im TFSI or TEGDME (Fig. 1d). The water molecules in all electrolytes exhibit an upfield shift compared to pure water, indicating an increased shielding effect of hydrogen atoms and higher external electron density. Specifically, under low water content conditions, strong cation–anion interactions in C_3C_1im TFSI prevent the formation of hydrogen bonds with H_2O, resulting in weak hydrogen bonding between C_3C_1im TFSI and H_2O.[39–41] In contrast, TEGDME forms stronger interactions with H_2O than those between H_2O molecules, as shown in Fourier transform infrared (FTIR) spectra (Fig. S2). The blue shifts of the H–O stretching and H–O–H bending suggest that TEGDME disturbs the hydrogen bond interaction between H_2O molecules.[42,43] Consequently, water exhibits the smallest chemical shift in TEGDME. Adding LiTFSI to C_3C_1im TFSI and TEGDME introduces a downfield shift in the chemical shift of H_2O due to the strong Lewis acidity of Li^+, which complexes with H_2O, enhances O–H bond polarity, and increases the deshielding effect.[44] Thus, the proton chemical shift in the C_3C_1im TFSI-based electrolyte is very close to that of free H_2O, which is favorable for inducing LiOH formation during discharge. X-ray

diffraction (XRD) analysis, as shown in Fig. 1e, confirmed that the C_3C_1im TFSI-based electrolyte could achieve LiOH detection (JCPDS No. 32-0564) under different water content conditions. In contrast, the TEGDME-based electrolyte failed to generate LiOH even at a high water content (6%), with Li_2O_2 being the predominant product instead. Moreover, the C_3C_1im TFSI-based electrolyte with higher water content promotes lower LiOH crystallinity compared to electrolytes with lower water content, as evidenced by less intense diffraction peaks corresponding to amorphous LiOH, which could effectively reduce the decomposition voltage.[45,46] UV-visible spectroscopy using titanium oxysulfate detection confirmed the absence of Li_2O_2 formation, indicating that the ionic liquid system consistently promotes LiOH-based chemistry rather than reverting to the typical Li_2O_2 formation (Fig. S3).[47,48] In contrast, the TEGDME-based electrolyte shows that Li_2O_2, as the discharge product, contributes more than half of the capacity under the same water content conditions (0.32 mAh *vs.* 0.5 mAh), similar to previous reports.[16,49] Water content also optimized the ionic conductivity in the ionic liquid system (Fig. S4 and Table S2). At 2% H_2O content, the ionic conductivity reaches 0.0322 mS cm^{-1}, sufficient for basic electrochemical operation but potentially limiting for high-rate applications. Increasing the water content to 6% provides optimal performance with a conductivity of 0.0579 mS cm^{-1}. Based on these comprehensive evaluations, 6% H_2O content in C_3C_1im TFSI was selected for subsequent studies, providing an optimal balance between ionic conductivity, LiOH decomposition efficiency, and electrochemical stability while ensuring adequate water supply throughout extended cycling (higher water content will result in electrolyte phase separation, as shown in Fig. S5).

Electrochemical characterization of PPD through cyclic voltammetry in the C_3C_1im TFSI electrolyte revealed a well-defined redox couple with an electrochemical potential of 3.55 V *vs.* Li/Li^+ (Fig. 2a). This potential is appropriately positioned 0.23 V above the theoretical LiOH formation voltage (3.32 V), providing sufficient thermodynamic driving force for chemical LiOH oxidation while maintaining a reasonable overpotential for energy efficiency optimization. The molecular architecture of PPD features a strategically designed p–π conjugation system between the nitrogen lone pair electrons and the benzene ring π-system. This conjugation provides several critical advantages: electronic delocalization stabilizes both the neutral and oxidized forms, and the planar aromatic system facilitates electron transfer. NMR spectroscopy analysis confirmed minimal interaction between PPD and both water and ionic liquid components, avoiding mediator sequestration that could compromise functionality (Fig. 2b). The ^{1}H-NMR signals of PPD showed negligible chemical shift changes (<0.02 ppm) in the presence of H_2O and C_3C_1im TFSI, indicating the absence of strong coordination effects or hydrogen bonding interactions. The weak interaction profile represents a marked departure from the behavior of traditional inorganic redox mediators, such as lithium iodide (LiI), which typically exhibit a pronounced tendency to coordinate with ionic liquids and water. This propensity for coordination often results in the sequestration of the redox mediator, thereby diminishing its availability for redox processes.[50,51] In contrast, the weak interaction between the electrolyte and PPD ensures sustained availability for redox reactions and maintains a high effective concentration throughout the electrolyte. Moreover, the absence of significant molecular interactions also eliminates potential complications from solvation effects that could alter redox potentials or create kinetic barriers to electron transfer. DFT calculations provided detailed molecular-level insights into PPD structure and electronic properties that explain its effectiveness as a redox mediator.[52] Geometry optimization revealed that PPD adopts a conformation where the nitrogen atom maintains sp^2 hybridization character with bond angles of approximately 120°, indicating significant p–π orbital overlap with the benzene ring system (Fig. 2c). Upon oxidation to PPD^+, the molecular structure undergoes only subtle changes (Fig. 2e). The C_{10}–N_{12} bond length decreases from 1.37 Å to 1.35 Å, indicating increased double-bond character and stronger p–π conjugation. Multiwfn analysis quantified the enhanced conjugation through Mayer bond order calculations, revealing an increase from 1.023 to 1.065 for the C_{10}–N_{12} bond upon oxidation (Table S3).[53–55] This increased bond order reflects enhanced electron sharing between the nitrogen atom and benzene ring, providing thermodynamic stabilization of the oxidized form, which is essential for reversible redox cycling. Surface electrostatic potential mapping revealed that the electron density distribution shifts significantly upon oxidation, with the negative potential region migrating from the nitrogen site toward the benzene ring in PPD^+ (Fig. 2d–f). This electronic reorganization facilitates charge stabilization through aromatic delocalization while maintaining molecular integrity, enabling PPD to undergo reversible single-electron oxidation without structural decomposition. The functional role of PPD^+ in modulating the oxygen evolution reaction (OER) is elucidated through thermodynamic analysis (Fig. 2g, h and Tables S4, S5). During the initial stage of oxidation, OH^- typically loses one electron and transforms into the reactive species OH*, where * denotes the active sites of free radical molecules. This transformation has traditionally been considered the onset of the OER process.[31,56,57] This initial oxidation of OH^- indicates an increase in Gibbs free energy of 4.804 eV (Fig. 2g). However, in the presence of PPD, a markedly different mechanism is enabled. PPD could be first oxidized to PPD^+, which subsequently engages in electron exchange with OH^-, facilitating a mediated electron transfer pathway. The optimized structure of mediated states of PPD and OH^- can be explained in the embedded figure in Fig. 2h. Across the three stages mentioned above, the free energy change pattern exhibits an initial increase followed by a decrease. ΔG_1 can be reduced to 1.368 eV in the step where the system loses one electron overall, which is roughly one-third of the direct electron loss by OH^-. This outcome highlights the catalytic effect of PPD^+ in lowering the OER activation barrier. The ΔG_2 for the subsequent reaction of PPD^+ with OH^- to form PPD: OH* is −0.369 eV, indicating that the oxidation step is the rate-determining step of the reaction and that the electron transfer to PPD^+ is a spontaneous process with decreasing free energy. The calculated energy change demonstrated that the electronic delocalization and inherent p–

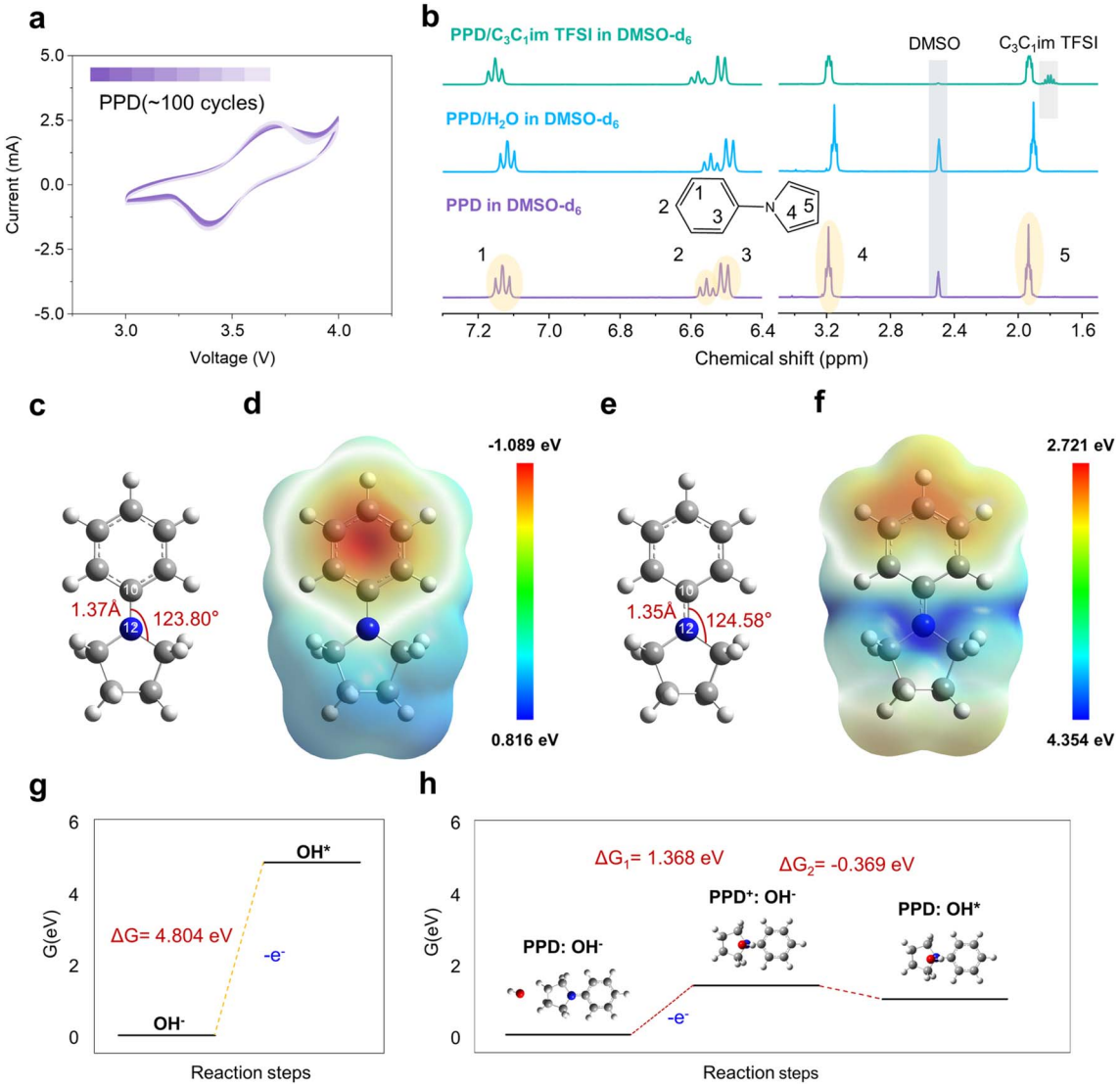

Fig. 2 (a) Extended cycles of cyclic voltammograms of 1 M LiTFSI/DMSO with 300 mM PPD at a scan rate of 10 mV s^{-1} in the potential range of 3.0–4.0 V under an Ar atmosphere. ^{1}H NMR spectra of (b) PPD in DMSO-d_6 with or without C_3C_1im TFSI and PPD in DMSO-d_6 with or without H_2O. The optimized structure of (c) PPD and (e) PPD^+. The surface electrostatic potential maps of (d) PPD and (f) PPD^+. (g) The Gibbs free energy change of OH^- at different valence states. (h) The Gibbs free energy change of the complex of PPD and OH^- at different redox states.

π conjugation within the PPD framework not only facilitate reversible redox cycling in solution but also modulate the interfacial energetics of hydroxide oxidation. This alternative pathway alleviates the kinetic limitations of direct OH^- oxidation, thereby enhancing the efficiency and durability of Li–O_2 battery systems during charging.

Experimental validation of mediator selectivity was performed through singlet oxygen detection experiments using 9,10-dimethylanthracene (DMA) as a molecular probe, as shown in Fig. S6. The characteristic decrease in DMA absorbance at 379 nm upon exposure to singlet oxygen confirmed that PPD does not function as a singlet oxygen scavenger, eliminating potential interference with oxygen-related chemistry through side reactions with reactive oxygen species. This selectivity is crucial because singlet oxygen scavenging could reduce mediator availability and create additional decomposition pathways that compromise cycling stability.[28,58,59] Discharge capacity testing demonstrated that PPD addition does not affect the normal discharge process, with similar capacities achieved in electrolytes with and without PPD (4148.8 *vs.* 3890.1 mAh g^{-1}, representing <7% variation within experimental error). Moreover, the presence or absence of PPD does not impact the normal formation of LiOH, as shown in Fig. S7. In contrast, the addition of H_2O could significantly affect the discharge process, as shown in Fig. S8. The discharge capacity in the anhydrous electrolyte is much lower than that in the hydrous electrolyte, implying that the proton composing LiOH comes from H_2O rather than ionic liquids or PPD. To explore the effect of PPD on the charging process, we observed the charging overpotentials of electrolytes with different PPD concentrations (Fig. S9), which showed no obvious correlation between charging overpotential and PPD concentration. Compared with the electrolyte

without PPD addition, both 25 mM and 50 mM PPD concentrations showed similar reduced charge overpotentials and improved stability. Charging experiments using LiOH pre-deposited cathodes provided direct mechanistic evidence for the chemical reaction pathway, compared with the conventional catalyst, ruthenium (Ru) metal (Fig. S10 and S11). Pre-deposited cathodes were prepared by discharging Li–O_2 batteries in an O_2 atmosphere to controlled capacities, followed by disassembly under inert conditions to preserve LiOH deposits (Fig. S12). When these cathodes were reassembled in fresh electrolyte containing PPD, the charging behavior showed a distinct stable plateau at the PPD oxidation potential, in contrast to the rising potential profile characteristic of direct electrochemical oxidation, as shown in Fig. S13. This stable charging plateau not only confirms that PPD^+ preferentially reacts with LiOH through chemical pathways rather than undergoing further oxidation to PPD^{2+} or other unstable high-valent states, as reported previously,[33] but also correlates with the initial oxidation potentials observed in the previous cyclic voltammograms (Fig. 2a). The theoretical capacity contribution from PPD oxidation alone (approximately 0.1 mAh based on mediator loading) is negligible compared to the observed LiOH decomposition capacity (1 mAh), supporting the chemical redox mediator mechanism. In the control experiment without PPD addition, the Ru-catalyzed charging curve exhibited a continuous increase in voltage. This trend indicates that Ru can only reduce the potential barrier of electrochemical reactions but cannot convert electrochemical reactions into chemical reactions. The persistent rise in voltage suggests that the electrochemical oxidation of LiOH requires an increasing overpotential as the reaction continues, rather than proceeding spontaneously through chemical pathways.

The critical importance of solvent compatibility becomes evident through systematic comparisons of PPD behavior in TEGDME and C_3C_1im TFSI electrolytes. These comparative studies revealed fundamental differences in redox mediator stability and cycling performance that directly correlate with solvent oxidative stability, providing crucial insights for mediator-electrolyte design principles. The optimized compositions of 25 mM PPD in the TEGDME-based electrolyte and C_3C_1im TFSI-based electrolyte are defined as E-PT and E-PC, respectively. At the molecular level, the imidazolium cation exhibits a lower HOMO and a higher oxidation potential compared to TEGDME, rendering it more resistant to oxidative attack by highly oxidizing species such as PPD^+ (Fig. 1b and c). Scanning electron microscopy (SEM) was used to assess morphological changes of the CNT cathode after 10 cycles in E-PT (Fig. 3a, b, S14, and S15). Compared to the pristine electrode with uniformly distributed CNT coverage on carbon cloth with individual nanotubes clearly visible and well-distributed across the substrate surface (Fig. S16), cycling in E-PT caused severe degradation: the active CNT material exhibited significant aggregation into large clusters and substantial detachment from the carbon cloth substrate, revealing the underlying bare carbon structure. This damage disrupts the three-phase reaction zone, reducing the active surface area and electron pathways, thus hindering oxygen electrochemistry. In stark contrast, E-PC maintained structural integrity under identical conditions (Fig. 3c, d, S17, and S18). The CNT active material remained well-adhered to the carbon cloth substrate after cycling, maintaining the individual nanotube morphology and uniform distribution essential for establishing effective electrochemical contact, preserving electrochemical contact, and preventing resistive layer formation. This enhanced stability in the ionic liquid electrolyte reflects suppressed parasitic reactions, ensuring consistent porosity and surface area throughout cycling and thereby sustaining battery performance. XRD patterns of cathodes cycled in E-PT revealed a complete absence of crystalline discharge products after 10 cycles, in stark contrast to the distinct Li_2O_2 peaks seen after the initial discharge (Fig. 3e and S19). This suggests that neither Li_2O_2 nor LiOH persists after cycling, likely due to full dissolution, amorphization, or extensive parasitic reactions. The lack of crystalline products underscores the incompatibility of PPD^+ with TEGDME during cycling. In contrast, E-PC consistently supports reversible LiOH chemistry, with sharp peaks at $2\theta = 32.4°$ and 35.6° maintained after multiple cycles (Fig. 3f and S20). These results confirmed that the PPD-ionic liquid system enables stable product formation and efficient round-trip reversibility by mitigating parasitic side reactions.

^{1}H-NMR analysis after cycling further provided direct spectroscopic evidence of extensive solvent degradation in E-PT, whereas no such degradation products were detected in E-PC, highlighting the superior stability of the ionic liquid system. The characteristic signals at 9.65 ppm and 8.42 ppm correspond to aldehyde and acetate functionalities, respectively, confirming the oxidative decomposition of the ether backbone through C–H bond cleavage and subsequent rearrangement reactions in E-PT (Fig. 3g). Additional peaks in the 4.0–4.5 ppm region indicate the formation of oxidized ether linkages and hemiacetal structures typical of partial ether oxidation. The accumulation of these degradation products throughout cycling progressively compromises electrolyte performance through multiple mechanisms: aldehyde species can react with lithium species to form passivating films,[60,61] carboxylic acid products can protonate basic components, and the consumption of the parent solvent reduces overall electrolyte volume and concentration. These cumulative effects explain the rapid performance degradation observed in E-PT. In contrast, E-PC showed minimal formation of degradation products after cycling (Fig. 3h and S21), providing compelling evidence for the chemical stability of the optimized system. After 10 cycles under identical conditions that completely degraded the E-PT, the characteristic aldehyde and acetate signals remained barely detectable even at 1000× magnification, representing less than 0.1% of the intensity observed in the degraded E-PT. The suppression of the aforementioned degradation products indicated that the stability of the electrolyte components was effectively preserved, which is crucial for the cycling process of air batteries because it minimizes performance degradation during cycling and could serve as an essential factor in maintaining the integrity of the three-phase interface.

The integrated electrochemical performance evaluation demonstrates the superior cycling capability achieved through the optimized PPD-ionic liquid combination. Li–O_2 batteries in

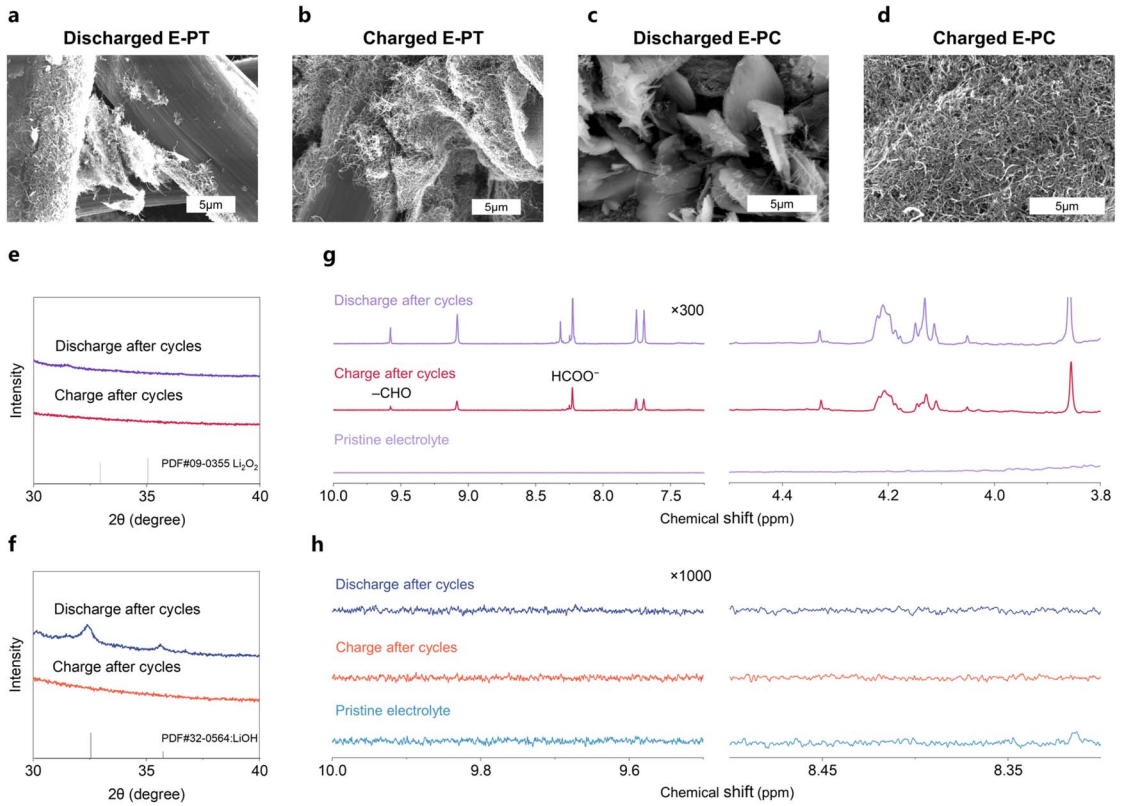

Fig. 3 SEM images of (a) the cathode after discharge and (b) cathode after charging in E-PT, and the (c) cathode after discharge and (d) cathode after charging in E-PC, respectively. XRD patterns of the cathodes after discharging and charging in (e) E-PT and (f) E-PC. ^{1}H NMR spectra of the pristine electrolyte, and the electrolyte after discharging and charging in (g) E-PT and (h) E-PC.

E-PC achieved 180 cycles at 100 mA g^{-1} with 500 mAh g^{-1} capacity limitation (Fig. 4a), representing an about ten-fold improvement over control systems without PPD addition (Fig. 4b). The voltage profiles revealed distinct mechanistic signatures that confirm chemical rather than electrochemical LiOH decomposition. The stable charging plateau at a potential slightly exceeding 3.8 V (Fig. 2a) indicates that the charging process occurs at the redox mediator potential rather than requiring higher overpotentials for direct electrochemical decomposition. This stable plateau contrasts with the rising

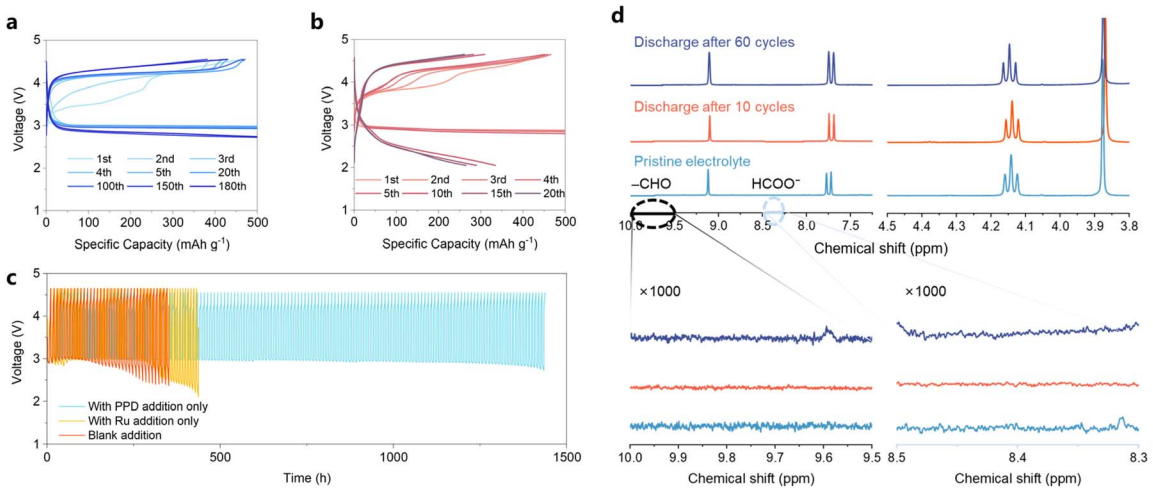

Fig. 4 Cycling performances of (a) a CNT cathode with PPD addition under a current density of 100 mA g^{-1} and a cut-off capacity of 500 mAh g^{-1}. Cycling performances of (b) a CNT cathode with blank addition under a current density of 100 mA g^{-1} and a cut–off capacity of 500 mAh g^{-1}. (c) Charge–discharge cycling performance of electrolytes with Ru or PPD catalysts. (d) ^{1}H NMR spectra of the pristine electrolyte and the electrolyte after the discharging process following different cycles.

potential profiles characteristic of electrochemical processes limited by charge transfer kinetics. Comparative studies with ruthenium-modified cathodes provide additional mechanistic insights. While the Ru catalyst reduces charging overpotentials through enhanced electrochemical kinetics, it maintains the fundamental electrochemical mechanism, as evidenced by the rising potential profiles during LiOH decomposition (Fig. S22). The limited cycling performance of Ru-catalyzed systems (30 cycles) compared to PPD-mediated systems demonstrates the superiority of chemical over electrochemical decomposition mechanisms for LiOH-based systems. The synergistic combination of PPD and Ru catalysts also achieved 150 cycles at the elevated capacity of 1000 mAh g^{-1} (Fig. S23), confirming that the chemical and electrochemical enhancement mechanisms can operate complementarily. The maintenance of a stable charging plateau at 3.8 V in the presence of both additives indicates that the chemical pathway dominates when PPD is available, with Ru providing additional electrochemical facilitation, as depicted in Fig. 4c.

Long-term stability assessment through 60-cycle testing demonstrated sustained performance without degradation indicators in E-PC (Fig. 4d). The consistent overpotentials and stable voltage profiles throughout extended cycling confirmed the durability of the E-PC and validated the chemical stability observed through spectroscopic analysis (Fig. S24). The comprehensive experimental evidence establishes that PPD functions as an effective redox mediator for LiOH-based Li–O_2 batteries when paired with appropriately stable ionic liquid electrolytes. The chemical decomposition mechanism enabled by this combination provides superior cycling performance compared to conventional electrochemical approaches, while the systematic solvent compatibility analysis provides design principles for future redox mediator development in advanced battery systems. Considering the reactivity of water and lithium metal in practical hydrous ionic liquid electrolytes, a binary copolymer reported previously,[62] composed of rigid acrylamide (AM) and flexible hexafluorobutyl (HFBA) acrylate units, which are rich in ester groups and abundant C–F moieties, was confirmed exhibiting superior water barrier properties in both Li–Li symmetric cells and a Li–O_2 battery in a C_3C_1im TFSI-based hydrous electrolyte (Fig. S25). These results demonstrate that the hydrophobic polymer layer can guarantee the normal operation of the batteries in hydrous ionic liquid-based electrolytes, thereby offering a promising solution to expand the applicability of Li–O_2 batteries.

Conclusions

We demonstrate that tailoring electrolyte activity through a synergistic pairing of PPD and ionic liquid electrolyte enables an efficient LiOH redox process in Li–O_2 batteries. The optimally tuned redox potential and robust p–π conjugation of PPD promote homogeneous chemical LiOH decomposition while preserving discharge chemistry. The ionic liquid not only suppresses parasitic mediator degradation but also steers discharge selectivity toward LiOH *via* controlled water–electrolyte interactions. This integrated molecular design transforms the charging pathway from sluggish, interface-limited electrochemistry to rapid solution-mediated reactions, delivering 180 stable cycles with reduced overpotentials. While our comprehensive structural and chemical analyses strongly corroborate the reversible LiOH chemistry, the direct quantification of the four-electron oxygen redox kinetics *via in situ* techniques, such as differential electrochemical mass spectrometry (DEMS), remains a critical next step. Ultimately, coupling tailored *in situ* diagnostic techniques with rational electrolyte engineering will provide a comprehensive understanding for broadening the practical use of Li–O_2 batteries. Beyond this, our results establish general design rules for mediator–electrolyte compatibility, highlighting thermodynamic matching as the key to long-term stability. This molecular-level framework offers a blueprint for engineering next-generation Li–O_2 systems and advances the broader pursuit of practical, high-energy rechargeable batteries.

Author contributions

X. D. Ren designed and guided this experiment. J. S. Guo helped perform the calculations. J. C. Yang did the electrochemical experiments and wrote the original draft. J. C. Yang, Z. H. Wang, and B-Q. Xiong conducted the material characterization. Jun. M and D. Z. Wang helped analyze the electrochemical results. X. D. Ren supervised the whole work and edited the manuscript.

Conflicts of interest

The authors declare no competing financial interest.

Data availability

Supplementary information (SI): experimental procedures, characterization methods, and results. See DOI: https://doi.org/10.1039/d5sc09544a.

Acknowledgements

This study was supported by the National Key R&D Program of China (2021YFA1201800) and the National Natural Science Foundation of China (Grant No. 92472125, 22179124). We acknowledge the resources from the Instruments Center for Physical Science, the Super Computing Center, and the Center for Micro and Nanoscale Research and Fabrication at USTC, as well as the Hefei Advanced Computing Center.

Notes and references

1 T. Liu, J. P. Vivek, E. W. Zhao, J. Lei, N. Garcia-Araez and C. P. Grey, *Chem. Rev.*, 2020, **120**, 6558–6625.
2 Z. Sun, X. Lin, C. Wang, Y. Tan, W. Dou, A. Hu, J. Cui, J. Fan, R. Yuan, M. Zheng and Q. Dong, *Adv. Mater.*, 2024, **36**, 2404319.
3 Z. Li, J. Wu, M. Li, D. Huang, K. Pan, Y. Dou, J. Wang, Z. Zhang and Z. Zhou, *Adv. Funct. Mater.*, 2025, 2501005.
4 P. G. Bruce, S. A. Freunberger, L. J. Hardwick and J.-M. Tarascon, *Nat. Mater.*, 2012, **11**, 19–29.

5 M. Armand and J. M. Tarascon, *Nature*, 2008, **451**, 652–657.
6 H.-M. Guan, Z.-P. Cai, X.-Y. Wu, K.-X. Wang and J.-S. Chen, *Angew. Chem., Int. Ed.*, 2025, e202509132.
7 U. Latif, *ACS Appl. Energy Mater.*, 2025, **8**, 4838–4883.
8 B. D. Adams, C. Radtke, R. Black, M. L. Trudeau, K. Zaghib and L. F. Nazar, *Energy Environ. Sci.*, 2013, **6**, 1772–1778.
9 L.-N. Song, L.-J. Zheng, X.-X. Wang, D.-C. Kong, Y.-F. Wang, Y. Wang, J.-Y. Wu, Y. Sun and J.-J. Xu, *J. Am. Chem. Soc.*, 2024, **146**, 1305–1317.
10 W. Liu, Y. Shen, Y. Yu, X. Lu, W. Zhang, Z. Huang, J. Meng, Y. Huang and Z. Guo, *Small*, 2019, **15**, 1900154.
11 J. Wang, Y. Zhang, L. Guo, E. Wang and Z. Peng, *Angew. Chem., Int. Ed.*, 2016, **55**, 5201–5205.
12 L. Dai, Q. Sun, Y. Yao, H. Guo, X. Nie, J. Li, P. Si, J. Lu, D. Li and L. Ci, *Sci. China Mater.*, 2022, **65**, 1431–1442.
13 T. Liu, M. Leskes, W. Yu, A. J. Moore, L. Zhou, P. M. Bayley, G. Kim and C. P. Grey, *Science*, 2015, **350**, 530–533.
14 Z. Gao, I. Temprano, J. Lei, L. Tang, J. Li, C. P. Grey and T. Liu, *Adv. Mater.*, 2023, **35**, 2201384.
15 T. Liu, Z. Liu, G. Kim, J. T. Frith, N. Garcia-Araez and C. P. Grey, *Angew. Chem., Int. Ed.*, 2017, **56**, 16057–16062.
16 X. Zhang, P. Dong, S. Noh, X. Zhang, Y. Cha, S. Ha, J.-H. Jang and M.-K. Song, *Angew. Chem., Int. Ed.*, 2023, **62**, e202212942.
17 M. C. Policano, C. G. Anchieta, T. C. M. Nepel, R. M. Filho and G. Doubek, *ACS Appl. Energy Mater.*, 2022, **5**, 9228–9240.
18 Y. Chen, S. A. Freunberger, Z. Peng, O. Fontaine and P. G. Bruce, *Nat. Chem.*, 2013, **5**, 489–494.
19 Z. Liu, Y. Zhang, C. Jia, H. Wan, Z. Peng, Y. Bi, Y. Liu, Z. Peng, Q. Wang, H. Li, D. Wang and J.-G. Zhang, *Nano Energy*, 2017, **36**, 390–397.
20 Z. Jiang, B. Wen, Y. Huang, Y. Wang, H. Fang and F. Li, *J. Am. Chem. Soc.*, 2025, **147**, 10992–10998.
21 J. Lu, Y. Jung Lee, X. Luo, K. Chun Lau, M. Asadi, H.-H. Wang, S. Brombosz, J. Wen, D. Zhai, Z. Chen, D. J. Miller, Y. Sub Jeong, J.-B. Park, Z. Zak Fang, B. Kumar, A. Salehi-Khojin, Y.-K. Sun, L. A. Curtiss and K. Amine, *Nature*, 2016, **529**, 377–382.
22 X. Hu, G. Luo, Q. Zhao, D. Wu, T. Yang, J. Wen, R. Wang, C. Xu and N. Hu, *J. Am. Chem. Soc.*, 2020, **142**, 16776–16786.
23 J. Lu, S. Dey, I. Temprano, Y. Jin, C. Xu, Y. Shao and C. P. Grey, *ACS Energy Lett.*, 2020, **5**, 3681–3691.
24 Z. Mohamed, Q. Zhou, K. Zhu, G. Zhang, W. Xu, P. J. Chimtali, Y. Cao, H. Xu, Z. Yan, Y. Wang, H. Akhtar, A. Al-Mahgari, X. Wu, C. Wang and L. Song, *Adv. Funct. Mater.*, 2025, **35**, 2410091.
25 C. Li, H. Luo, F. Li and F. Li, *ACS Omega*, 2023, **8**, 45348–45357.
26 X. Bi, M. Li, C. Liu, Y. Yuan, H. Wang, B. Key, R. Wang, R. Shahbazian-Yassar, L. A. Curtiss, J. Lu and K. Amine, *Angew. Chem., Int. Ed.*, 2020, **59**, 22978–22982.
27 X. Gao, Y. Chen, L. Johnson and P. G. Bruce, *Nat. Mater.*, 2016, **15**, 882–888.
28 W.-J. Kwak, H. Kim, Y. K. Petit, C. Leypold, T. T. Nguyen, N. Mahne, P. Redfern, L. A. Curtiss, H.-G. Jung, S. M. Borisov, S. A. Freunberger and Y.-K. Sun, *Nat. Commun.*, 2019, **10**, 1380.
29 J.-B. Park, S. H. Lee, H.-G. Jung, D. Aurbach and Y.-K. Sun, *Adv. Mater.*, 2018, **30**, 1704162.
30 Q. Xiong, G. Huang and X.-B. Zhang, *Angew. Chem., Int. Ed.*, 2020, **59**, 19311–19319.
31 C. Rong, X. Huang, H. Arandiyan, Z. Shao, Y. Wang and Y. Chen, *Adv. Mater.*, 2025, **37**, 2416362.
32 Z. Peng, *Nat. Chem.*, 2023, **15**, 1206–1208.
33 H.-D. Lim, B. Lee, Y. Zheng, J. Hong, J. Kim, H. Gwon, Y. Ko, M. Lee, K. Cho and K. Kang, *Nat. Energy*, 2016, **1**, 16066.
34 A. R. Neale, R. Sharpe, S. R. Yeandel, C.-H. Yen, K. V. Luzyanin, P. Goddard, E. A. Petrucco and L. J. Hardwick, *Adv. Funct. Mater.*, 2021, **31**, 2010627.
35 S. Wu, J. Tang, F. Li, X. Liu, Y. Yamauchi, M. Ishida and H. Zhou, *Adv. Funct. Mater.*, 2016, **26**, 3291–3298.
36 E. Knipping, C. Aucher, G. Guirado and L. Aubouy, *New J. Chem.*, 2018, **42**, 4693–4699.
37 S. S. H. Zaidi and X. Li, *Adv. Energy Mater.*, 2023, **13**, 2300985.
38 X. Tang, S. Lv, K. Jiang, G. Zhou and X. Liu, *J. Power Sources*, 2022, **542**, 231792.
39 N.-N. Wang, Q.-G. Zhang, F.-G. Wu, Q.-Z. Li and Z.-W. Yu, *J. Phys. Chem. B*, 2010, **114**, 8689–8700.
40 I. Khan, M. Taha, S. P. Pinho and J. A. P. Coutinho, *Fluid Phase Equilib.*, 2016, **414**, 93–100.
41 M. Sha, H. Dong, F. Luo, Z. Tang, G. Zhu and G. Wu, *J. Phys. Chem. Lett.*, 2015, **6**, 3713–3720.
42 Y. Shang, N. Chen, Y. Li, S. Chen, J. Lai, Y. Huang, W. Qu, F. Wu and R. Chen, *Adv. Mater.*, 2020, **32**, 2004017.
43 M. Shangguan, K. Wang, Y. Zhao and L. Xia, *Batteries*, 2023, **9**, 462.
44 M. Chen, J. Wu, T. Ye, J. Ye, C. Zhao, S. Bi, J. Yan, B. Mao and G. Feng, *Nat. Commun.*, 2020, **11**, 5809.
45 Y. Wang, N.-C. Lai, Y.-R. Lu, Y. Zhou, C.-L. Dong and Y.-C. Lu, *Joule*, 2018, **2**, 2364–2380.
46 A. Dutta, K. Ito, A. Nomura and Y. Kubo, *Adv. Sci.*, 2020, **7**, 2001660.
47 X. Ren, K. C. Lau, M. Yu, X. Bi, E. Kreidler, L. A. Curtiss and Y. Wu, *ACS Appl. Mater. Interfaces*, 2014, **6**, 19299–19307.
48 C. Zhang, S. Wang, T. Yang, N. Shan, S. K. Singh, A. Jaradat, M. K. Ncube, P. Redfern, A. Subramanian, Z. Huang, A. T. Ngo, L. A. Curtiss and A. Salehi-khojin, *Energy Storage Mater.*, 2023, **60**, 102844.
49 S. Ma, J. Wang, J. Huang, Z. Zhou and Z. Peng, *J. Phys. Chem. Lett.*, 2018, **9**, 3333–3339.
50 I. Temprano, T. Liu, E. Petrucco, J. H. J. Ellison, G. Kim, E. Jónsson and C. P. Grey, *Joule*, 2020, **4**, 2501–2520.
51 X. Bi, J. Li, M. Dahbi, J. Alami, K. Amine and J. Lu, *Adv. Mater.*, 2022, **34**, 2106148.
52 M. J. e. Frisch, G. W. Trucks, H. B. Schlegel, G. E. Scuseria, M. Robb, J. R. Cheeseman, G. Scalmani, V. Barone, G. A. Petersson and H. Nakatsuji, *Gaussian, Inc.*, Wallingford, CT, 2016.
53 T. Lu and F. Chen, *J. Comput. Chem.*, 2012, **33**, 580–592.
54 I. Mayer, *Chem. Phys. Lett.*, 1983, **97**, 270–274.
55 I. Mayer, *Int. J. Quantum Chem.*, 1984, **26**, 151–154.
56 W. Zhang, J. Zheng, R. Wang, L. Huang, J. Wang, T. Zhang and X. Liu, *Small*, 2023, **19**, 2301391.

57 X. Ren, T. Wu, Y. Sun, Y. Li, G. Xian, X. Liu, C. Shen, J. Gracia, H.-J. Gao, H. Yang and Z. J. Xu, *Nat. Commun.*, 2021, **12**, 2608.
58 Z. Jiang, Y. Huang, Z. Zhu, S. Gao, Q. Lv and F. Li, *Proc. Natl. Acad. Sci. U. S. A*, 2022, **119**, e2202835119.
59 J. Wandt, P. Jakes, J. Granwehr, H. A. Gasteiger and R.-A. Eichel, *Angew. Chem., Int. Ed.*, 2016, **55**, 6892–6895.
60 E. W. C. Spotte-Smith, R. L. Kam, D. Barter, X. Xie, T. Hou, S. Dwaraknath, S. M. Blau and K. A. Persson, *ACS Energy Lett.*, 2022, **7**, 1446–1453.
61 M. Schellenberger, R. Golnak, W. G. Quevedo Garzon, S. Risse and R. Seidel, *Mater. Today Adv.*, 2022, **14**, 100215.
62 J. Luo, Q. Huang, D. Shi, Y. Qiu, X. Zheng, S. Yang, B. Li, J. Weng, M. Wu, Z. Liu, Y. Yu and C. Yang, *Adv. Funct. Mater.*, 2024, **34**, 2403021.